Supporting Information

Modular, Multi-Robot Integration of Laboratories: An Autonomous Solid-State Workflow for Powder X-Ray Diffraction

Amy. M. Lunt,[1,2] Hatem Fakhruldeen,[1] Gabriella Pizzuto,[1] Louis Longley,[1] Alexander White,[1] Nicola Rankin,[1,2] Rob Clowes,[1] Ben Alston,[1,2] Lucia Gigli,[3] Graeme M. Day,[3] Andrew I. Cooper[1,2]* and Samantha Y. Chong[1,2]*

[1] Department of Chemistry and Materials Innovation Factory, University of Liverpool, L7 3NY, UK. E-mail: aicooper@liverpool.ac.uk, schong@liverpool.ac.uk

[2] Leverhulme Research Centre for Functional Materials Design, University of Liverpool, Liverpool L7 3NY, UK

[3] Computational Systems Chemistry, School of Chemistry, University of Southampton, SO17 1BJ, UK

Contents

1. Supporting Videos

Video 1 (6 min 16 sec, recorded at 4K resolution): Captioned video overview of the 12 stages of the autonomous PXRD workflow described in Fig. 1 in the main paper, along with the associated text. Note that the video is accelerated by varying degrees at different stages of the workflow, but the average acceleration is approximately x 10. An unaccelerated version of this Video without captions (55 min 29 sec) is included below. Benzimidazole was the test substance used in these experiments.

YouTube link: https://youtu.be/8rnaoTF-VMk

Original video file (downloadable):
https://www.dropbox.com/s/riq3jktroa74dbs/PXRD_6%27_16%22_captions_4K.mp4?dl=0

The key steps in the workflow can be found at the following points in **Video 1** (*note these are also marked as clickable **time stamps** in the online video*).

0 min 0 sec	**Step 1:** KUKA robot collects a rack of 8 crystalline samples from the Chemspeed platform.
0 min 24 sec	**Step 2:** Mobile KUKA manipulator delivers the rack of 8 samples to the preparation station, which involves a dual-arm ABB YuMi robot.
1 min 6 sec	**Step 3:** Dual-arm YuMi robot transfers the 8 samples to grinding station 1, where they are reduced in size using mechanical attrition (magnetic stirring).
1 min 40 sec	**Step 4:** The YuMi robot inverts the 8 samples and transfers them to grinding station 2; agitation reduces particle size further and transfers the sample onto the adhesive Kapton polymer film in the vial cap.
2 min 26 sec	**Step 5:** the YuMi robot inverts the samples again and transfers them to the X-ray diffraction plate.
2 min 51 sec	**Steps 6 & 7:** The YuMi robot unscrews each sample-loaded vial cap, inverts it, and places it back into the PXRD plate.
4 min 19 sec	**Step 8:** KUKA robot collects PXRD plate containing the 8 samples.
4 min 32 sec	**Step 9:** KUKA robot transports the sample plate to the powder X-ray diffractometer.
4 min 51 sec	**Step 10:** KUKA robot opens the doors of the X-ray diffractometer.
5 min 3 sec	**Step 11:** KUKA robot transfers the X-ray plate into the diffractometer.
5 min 26 sec	**Step 12:** KUKA closes the doors of the X-ray diffractometer and diffraction data are collected.
5 min 51 sec	KUKA robot opens doors and retrieves the X-ray plate from the diffractometer.

Video 2 (55 min 29 sec, recorded at 4K resolution): Video showing full workflow run including sample processing, transport, and PXRD data acquisition with no acceleration and no captions. Note that neither of these Videos shows the initial sample preparation step (liquid dispensing and evaporation) that is carried out by the Chemspeed platform (Figures S1 & S2) prior to grinding, sample mounting and PXRD analysis; both videos start at the point where crystals have already been grown. To introduce multiple camera angles, we recorded video footage from more than one run and merged them to create the videos shown here. The timings do not vary significantly between runs. Note also that the PXRD acquisition time is artificially short for the purposes of video capture; the actual acquisition time to produce the data shown in the manuscript was approximately one hour per sample.

YouTube link: https://youtu.be/cKAELaBfqEI

Original video file (downloadable):
https://www.dropbox.com/s/x2xoej9cceovczk/Amy_WF_full_54%27_29"_no_captions.mp4?dl=0

2. Experimental Methods

PXRD. Diffraction data were collected using a Panalytical X'Pert Pro diffractometer that was controlled using a Panalytical-developed software package comprising X'Pert Data Collector and X'pert Operator Interface. The X'Pert Data Collector directly communicates with the instrument and controls the instrumental parameters, such as opening and closing the shutter for the X-ray tube, the height and position of the stage and assigning the correct geometric setup. Datasets were collected in transmission mode over the range 4 to 40 in two theta in approximately 0.013 degree steps over 60 minutes. Le Bail refinement (*1*) for both the robotic and manual data was done (by hand) using TOPAS academic software (*2*), both for benzimidazole (*3*) and for ROY (*4*). All patterns were fitted in the range $10 \leq 2\theta \leq 40°$. Backgrounds were modelled using a Chebyshev polynomial with 10 coefficients and the peak shapes were described using a modified Thompson-Cox-Hastings pseudo-Voigt profile, with a single parameter used to model asymmetry due to axial beam divergence.

KUKA KMR iiwa mobile robot manipulator: This KUKA mobile robot comprises two connected robots; a robotic arm mounted on top of mobile base. Together, these units were controlled using the KUKA software framework, SunriseOS3, which features the arm manipulations and a complete navigation package for the base. The programs within the software framework are written in the Java programming language. Positions of the joints were saved as coordinates in frames, which can be called within the software. The position of the robot base is determined by x and y coordinates (that is, its position on the map, see Figure 2, main text) and the angle θ (its orientation). Transitions between saved frames were either linear (LIN), or the calculated most efficient path between the two points (PTP). The KUKA arm has seven degrees of freedom and a maximum payload of 14 kg, which is more than adequate for the tasks described here. The mobile base has a maximum speed of 3 km h^{-1} and can carry payloads of up to 200 kg. It can navigate a laboratory setting by using 2D laser scanner, which produce the map of the laboratory that is shown in Figure 2 (main text). To navigate the laboratory, several user defined positions or 'way points' were created (circled numerals in Fig. 2). These locations were taught to the robot by saving their coordinates to

the base. This allows easier path planning and control of the mobile base. The robot also has a range of safety features, including collision detection for both the arm and the base. For the arm, this is activated when a force of 30 N or greater is detected and this results in the arm stopping immediately. For the base, the laser scanners control how close a user can get to the robot (this distance varies with the robot speed); below this distance threshold there is an emergency stop. This emergency stopping also applies if the map changes for the robot and there is an unexpected object in its path.

IRB 14000 YuMi dual-arm robot: This is a dual-armed robot supplied by ABB Robotics. Each independent arm has seven axes and can accommodate interchangeable grippers. This makes this robot suitable for a wide range of applications, including assembly, pick and place operations, and packaging. The robot was fitted with ABB Robotics' SmartGripper as an end effector on each arm. Each end effector has two flat fingers for grasping. Here, neoprene adhesive tape was added to each finger, to assist with gripping and grasping of different object shapes and different materials. The YuMi robot was controlled using the ABB RobotStudio software, which is a manufacturer specific text-based programming language (see Figure S11 for an example of this code). The programming can be done through a tablet, which allows the operator to teach the robot new tasks by guiding its arms through the desired movements. As for the KUKA cobot, this robot has safety features and stops if an unexpected force is encountered, although the force-generating capability of the YuMi robot is much lower than for the KUKA robot.

Chemspeed FLEX LIQUIDOSE liquid dispensing platform: A Chemspeed FLEX LIQUIDOSE platform was used for dispensing accurate volumes of stock solutions into glass sample vials prior to crystallization, and for screw-capping the sample vials once the crystallization solvent had evaporated. The platform was controlled using Chemspeed's AutoSuite software package. The automated door on the front of this platform slides vertically, up and down, and can be controlled in the AutoSuite package, thus allowing the KUKA robot to access the samples unattended. The XYZ gantry robot in the platform moves in three directions allowing access to the whole platform; it has two interchangeable heads—the needle head and the screw capper tool. Changing between the heads is automated within the platform. The deck layout can be changed to accommodate custom designs for rack holders depending on the user's requirements (see Figure S2, below). The whole platform is connected to an extraction outlet to ensure safety when dispensing organic solvents.

Grinding station 1: The station reduces the particle size of the crystals using a Telfon-coated magnetic stirrer that is in each sample vial. The station comprises an IKA Digital Hotplate with a custom-designed 8-position 3D printed sample vial holder.

Grinding station 2: This station reduces the particle size further by shaking (IKA Vibrax Shaker Plate) and, more importantly, transfers the powder onto the adhesive Kapton film in the vial lid. The samples were inverted by the YuMi robot prior to shaking to facilitate this. The robot adds a lid to the samples prior to shaking (2 min 14 sec in **Video 1**) to retain the sample vials.

3. Crystal Structure Prediction Methods

Candidate crystal structures of ROY were taken from previously reported data (*5*).

Candidate crystal structures of benzimidazole were generated via Crystal Structure Prediction (CSP) with the following procedure.

The gas-phase molecular structure of benzimidazole was optimised at the PBE0/6-311G** level of theory using Gaussian 09 (*7*). The molecular structure was kept rigid during the CSP structure generation process.

Distributed, atom-centred multipoles up to hexadecapole were derived from the PBE0/6-311G** electron density by a distributed multipole analysis and partial charges were fitted to the multipoles (*8*–*10*). DMACRYS (*11*) was used with an anisotropic atom-atom force-field energy model for all lattice energy minimisations. Lattice energies were calculated using the FIT (*7*) force field and molecular charge densities were computed from a distributed multipole analysis (DMA) (*8*).

A quasi-random search of the crystal packing space was conducted in the most commonly observed space groups (SG) for organic molecular crystals using the Global Lattice Energy Explorer (GLEE) (*14*) software. The space groups analysed for Z'=1 and Z'=2 were:

Z'=1 (non-chiral)			Z'=2		
SG number	SG name	# structures	SG number	SG name	# structures
14	P 1 2_1 / c 1	20000	2	P -1	40000
19	P 2_1 2_1 2_1	10000	14	P 1 2_1 / c 1	100000
2	P -1	10000	4	P 1 2_1 1	40000
4	P 1 21 1	10000	19	P 2_1 2_1 2 1	40000
61	P b c a	10000	1	P 1	20000
15	C 1 2 / c 1	20000	29	P c a 2_1	10000
33	P n a 2_1	10000	33	P n a 2_1	10000
9	C 1 c 1	10000	15	C 1 2 / c 1	10000
29	P c a 2_1	10000	61	P b c a	10000
5	C 1 2 1	10000	5	C 1 2 1	10000
1	P 1	10000	9	C 1 c 1	10000
60	P b c n	10000	7	P 1 c 1	10000
7	P 1 c 1	10000	18	P 2_1 2_1 2	10000
18	P 2_1 2_1 2	10000			
96	P 4_3 2_1 2 & P 4_1 2_1 2	10000			
76	P 4_1 & P 4_3	10000			
145	P 3_2 & P 3_1	10000			
43	F d d 2	10000			
56	P c c n	10000			
13	P 1 2 / c 1	10000			
169	P 6_1 & P 6_5	10000			
88	I 4_1 / a	10000			
148	R -3	10000			
20	C 2 2 2_1	10000			
86	P 4_2 / n	10000			
154	P 3_2 2 1 & P 3_1 2 1	10000			

A total of 600,000 valid structures (280,000 and 320,000 for Z'=1 and Z'=2) were lattice energy minimised using the software package PMIN (*15*), followed by DMACRYS (*10*).

Duplicates were removed from the obtained set of structures. Initially, structures were clustered within each space group by comparison of simulated PXRD patterns generated by PLATON (*16*), obtaining 49,680 (3096 and 46,584 for Z'=1 and Z'=2) structures. Then, an additional clustering using the COMPACK algorithm (*17*) was performed only on the structures within a window of 12 kJ mol^{-1} above the global minimum energy structure (1042, of which 98 and 944 for Z'=1 and Z'=2). The final set contained 961 structures (76 and 885 for Z'=1 and Z'=2).

The resulting set of 961 structures was re-optimised by plane-wave-based periodic DFT (pDFT) using the VASP package (*18,19*). The re-optimisation was performed following a three-step procedure that has been observed to accelerate the convergence of pDFT optimisations for organic crystal structures (*20*). In the first step, only atomic positions are optimised, in the second, both atomic positions and unit-cell parameters are optimised, and in the third, a final single-point calculation is performed. All VASP calculations were performed using the PBE exchange-correlation function with the Becke-Johnson-damped Grimme dispersion (GD3BJ) correction (*21,22*).

The reoptimized 961 structures were clustered using the COMPACK algorithm (17), obtaining a final set of 902 structures.

PXRD comparison was performed using the variable-cell powder difference (VC-PWDF) method (*23*). The experimental PXRD patterns were background-corrected using DASH (*24*). The 2 range was truncated at 10° (to avoid the peaks from the adhesive Kapton tape; see Figure 3A and Figure 4A,B,D in main text), and at 40° and 35° for benzimidazole and ROY, respectively.

3. Supporting Figures (x 14) & Tables (x 4)

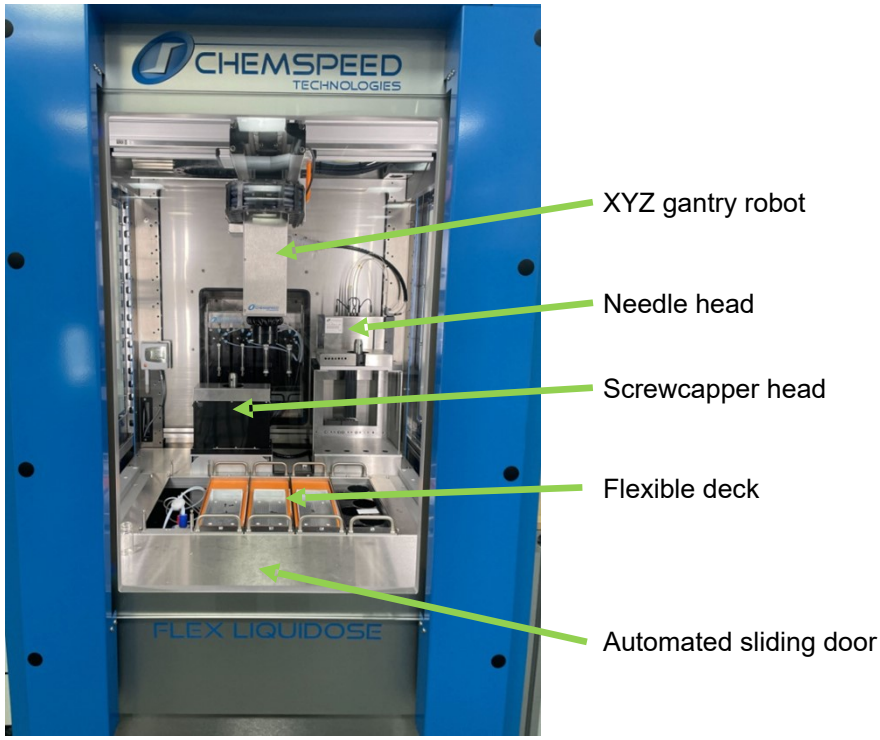

Figure S1: Chemspeed FLEX LIQUIDOSE platform, highlighting the vertical automated sliding door, the interchangeable needle and screw-capper heads, the flexible deck layout, and the XYZ gantry robot for sample transport.

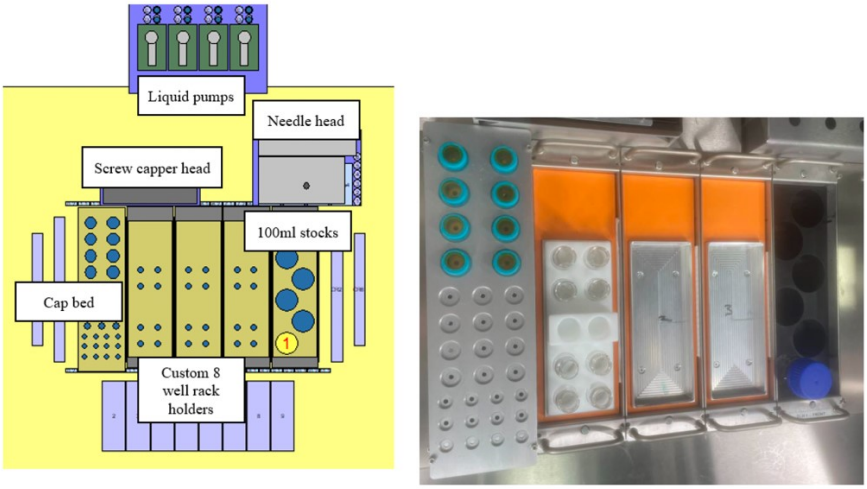

Figure S2: Left: Screenshot of the deck layout of the workflow, taken from the AutoSuite software. Right: Photograph of the equivalent deck layout in the Chemspeed FLEX LIQUIDOSE platform, with one occupied and two empty 8-vial racks. The Kapton-film vial caps are preloaded in the rack on the left.

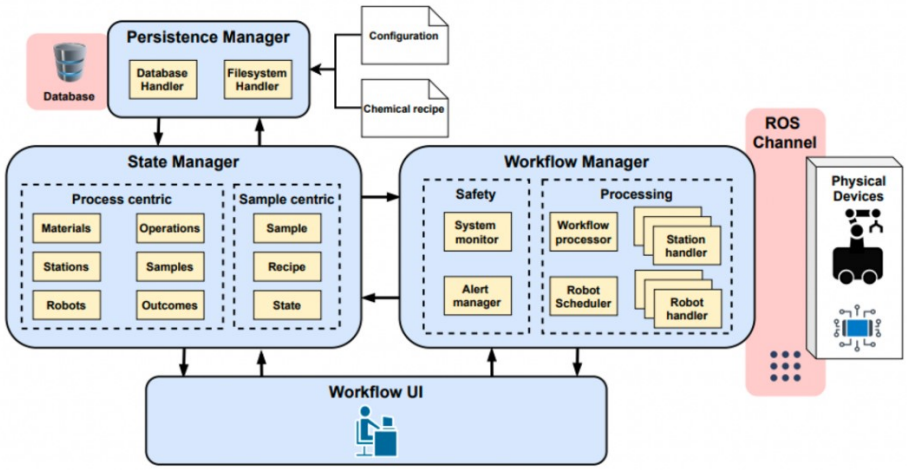

Figure S3: Block diagram summary of ARChemist software used to orchestrate the workflow (ref. 29, main text). The *State Manager* is responsible for representing the chemistry experiment state. The *Persistence Manager* allows the storage and retrieval of this state from a database and is responsible for parsing the input files. The *Workflow Manager* processes the experiment samples and assigns them to their respective robots and stations. The architecture uses ROS as a communication layer to interact with the physical robots and lab equipment. The *Workflow User Interface* allows the scientist to interact with the system and provide their input.

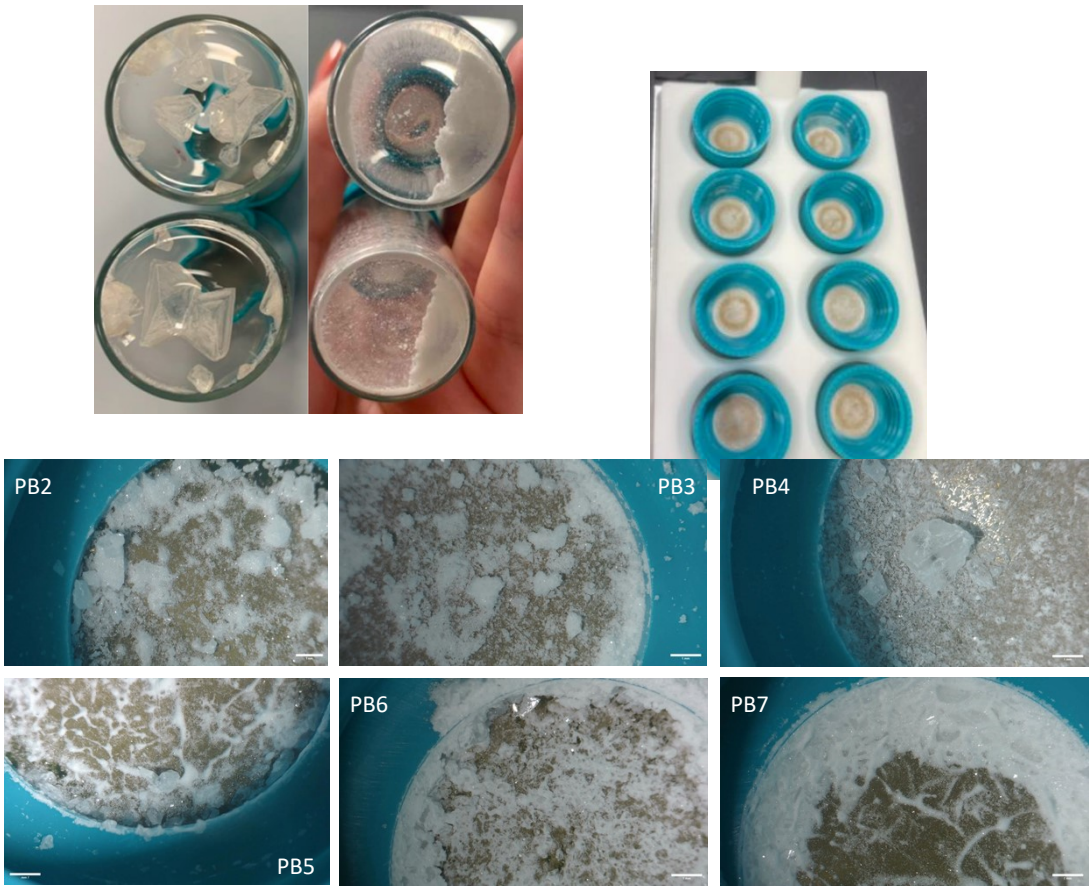

Figure S4: Upper left: Photograph comparing typical benzimidazole crystals as grown from methanol by evaporation in a glass vial, which are strongly adhered to the vial wall. **Upper center:** The same samples after automated grinding, which involved two minutes stirring and two minutes shaking with a standard magnetic stirrer in each vial (Steps 3 & 4 in Figure 1, main text). **Upper right:** Photograph showing the PXRD plate after robotic sample preparation of the benzimidazole crystals. The plate contains the 8 caps, each with an adhesive Kapton tape film (Figure S5). As described in Figure 1 and main text (see also Video 1), the robotic workflow has reduced the particle size of the large benzimidazole crystals and grinding station 2 (see Steps 4 & 5 in Figure 1, main text) has coated each film with a light dusting of the powdered benzimidazole material, which adheres to the Kapton tape.

Lower (6 images): Optical microscope images of samples produced by automated grinding (scale bar = 1 mm). While the particle size is clearly reduced (*c.f.*, Upper Left), some larger aggregates are still present (*e.g.*, in sample PB4), suggesting that further improvements to the grinding step are still possible, perhaps using longer grinding times or more intensive mechanical agitation.

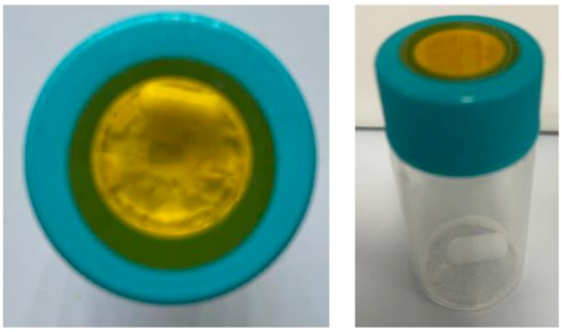

Figure S5: Photograph showing glass sample vials with a Kapton film covering the septum vial cap. The adhesive side of the Kapton film faces into the sample vial.

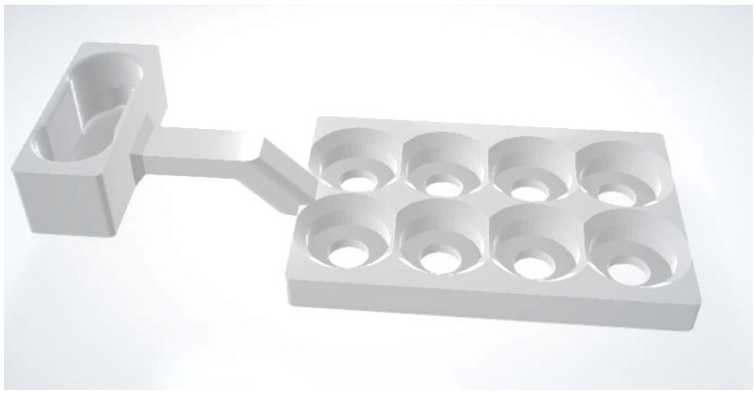

Figure S6: Design for the final prototype of the PXRD sample plate, which includes a custom handle that is complementary to the robot end effectors (see *e.g.*, manipulations in **Video 1**, 4 min 20 sec and 5 min 12 sec). The same design for robot grasping was also used for the sample transport plate (see 0 min 13 sec in **Video 1**). The eight sample holes are chamfered to allow easy loading of the sample caps.

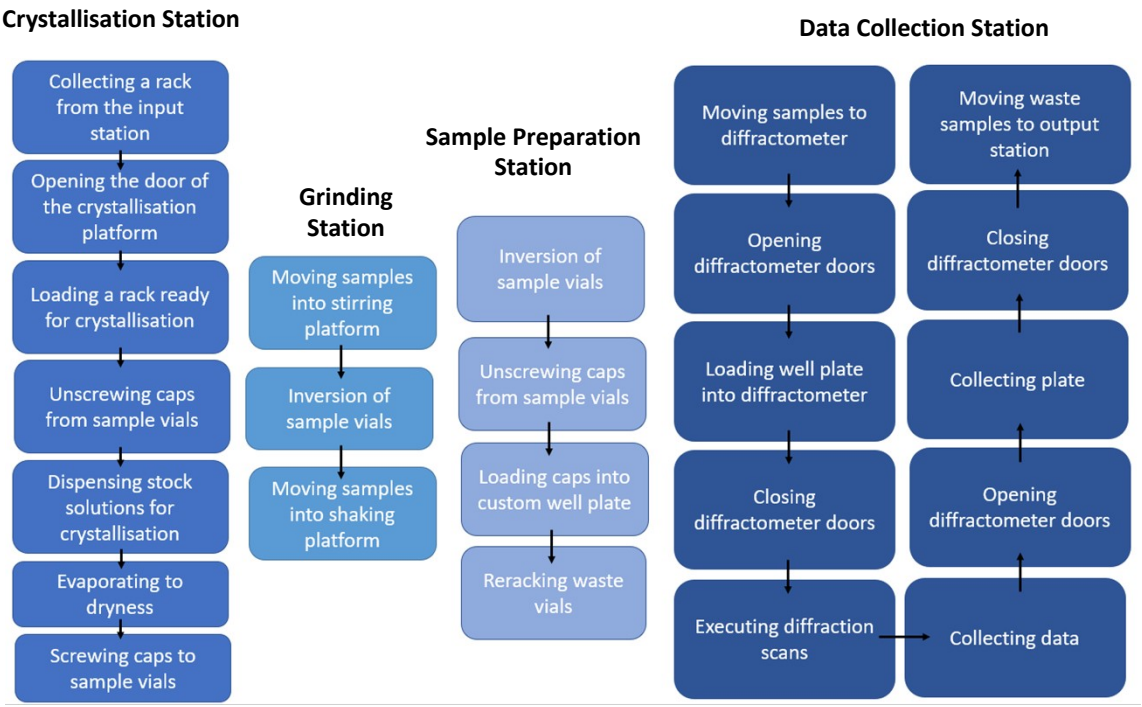

Figure S7: Flow diagram summarizing the various steps in the autonomous workflow.

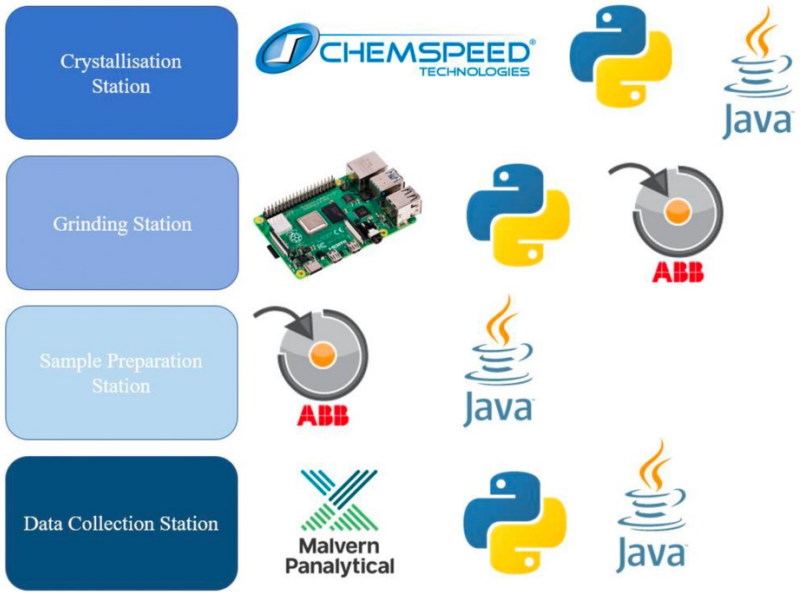

Figure S8: Overview of the control protocols and programming languages used for each station in the workflow. The images depict Chemspeed Autosuite GUI, Python programming language, Java programming language, Raspberry Pi microcontroller, ABB RobotStudio GUI and Malvern Panalytical GUI.

```
[ShakerPlateStation_22]: Current state changed to StationState.WAITING_ON_ROBOT
[WorkflowManager]: KukaLBRTask with task: UnloadPXRDRackYumiStation, params: ['True'] @(30, 1) is added to robot sch
eduling queue.
[KukaLBRIIWA_1]: Job (KukaLBRTask with task: UnloadPXRDRackYumiStation, params: ['True'] @(30, 1)) is assigned.
[KukaLBRIIWA_1]: Current state changed to RobotState.OP_ASSIGNED
[KukaLBRIIWA_1]: Job (KukaLBRTask with task: UnloadPXRDRackYumiStation, params: ['True'] @(30, 1)) is retrieved.
[KukaLBRIIWA_1]: Current state changed to RobotState.IDLE
[WorkflowManager]: KukaLBRIIWA_1 finished executing job KukaLBRTask with task: UnloadPXRDRackYumiStation, params: ['
True'] @(30, 1)
[WorkflowManager]: Notifying ShakerPlateStation_22
[ShakerPlateStation_22]: Robot job request is fulfilled.
[ShakerPlateStation_22]: Current state changed to StationState.PROCESSING
[ShakerPlateStation_22]: Robot job request for (KukaLBRTask with task: UnloadEightWRackYumiStation, params: ['False'
] @(30, 1)) is retrieved.
[ShakerPlateStation_22]: Current state changed to StationState.WAITING_ON_ROBOT
[WorkflowManager]: KukaLBRTask with task: UnloadEightWRackYumiStation, params: ['False'] @(30, 1) is added to robot
scheduling queue.
[KukaLBRIIWA_1]: Job (KukaLBRTask with task: UnloadEightWRackYumiStation, params: ['False'] @(30, 1)) is assigned.
[KukaLBRIIWA_1]: Current state changed to RobotState.OP_ASSIGNED
[KukaLBRIIWA_1]: Job (KukaLBRTask with task: UnloadEightWRackYumiStation, params: ['False'] @(30, 1)) is retrieved.
[KukaLBRIIWA_1]: Current state changed to RobotState.IDLE
[WorkflowManager]: KukaLBRIIWA_1 finished executing job KukaLBRTask with task: UnloadEightWRackYumiStation, params:
['False'] @(30, 1)
[WorkflowManager]: Notifying ShakerPlateStation_22
[ShakerPlateStation_22]: Robot job request is fulfilled.
[ShakerPlateStation_22]: Current state changed to StationState.PROCESSING
```

```
[KukaLBRIIWA_1]: Job (KukaLBRTask with task: LoadPXRDRackYumiStation, params: ['False'] @(30, 1) is
complete.
[KukaLBRIIWA_1]: Current state changed to RobotState.EXECUTION_COMPLETE
[IkaPlateDigital_23]: Requesting robot job (YuMiRobotTask with task: loadIKAPlate, params: [] @(30,
1))
[IKAStirPlateSm]: current state is load_stir_plate
[YuMiRobot_123]: Current state changed to RobotState.EXECUTING_OP
[INFO] [1684325354.275454]: executing loadIKAPlate
[YuMiRobot_123]: Job (YuMiRobotTask with task: loadIKAPlate, params: [] @(30, 1) is complete.
[YuMiRobot_123]: Current state changed to RobotState.EXECUTION_COMPLETE
[IkaPlateDigital_23]: Current state changed to StationState.OP_ASSIGNED
[IkaPlateDigital_23]: Requesting station job (<archemist.stations.ika_digital_plate_station.state.IK
AStirringOpDescriptor object at 0x7f86408e7430>)
[IKAStirPlateSm]: current state is stir
[IkaPlateDigital_23]: Current state changed to StationState.EXECUTING_OP
[INFO] [1684325396.002056]: executing stirring operation
[IkaPlateDigital_23]: Station op is complete.
[IkaPlateDigital_23]: Current state changed to StationState.PROCESSING
```

Figure S9: Two screenshots showing examples of the command line interface where the ARChemist server is launched (upper) and command line interface for the Handler's execution logs (lower). See Figure S3 for the general ARChemist overview.

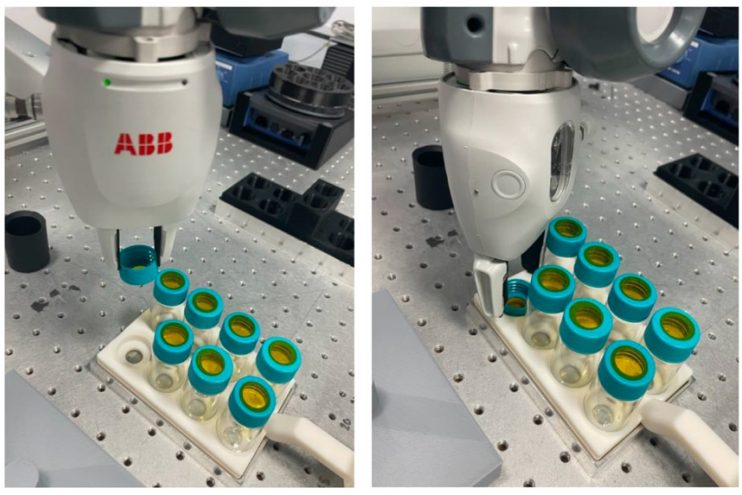

Figure S10: Photograph showing ABB YuMi robot placing a sample cap into the PXRD sample holder (Figure S3. In this test the sample vials are empty; when loaded with sample, the Kapton film becomes opaque (see *e.g.*, **Video 1**, 2 min 40 sec *et seq.*).

```
! unscrew
    FOR i FROM 1 TO 8 DO
        g_GripIn \holdForce:=10;
        MoveL RelTool (CRobT(\Tool:=GripperR),0,0,-1,\Rz:=-95), v200, z50,GripperR;
        WaitRob \ZeroSpeed;
        g_GripOut \holdForce:=10;
        MoveL RelTool (CRobT(\Tool:=GripperR),0,0,0,\Rz:=95), v200, z50,GripperR;
        WaitRob \ZeroSpeed;
    ENDFOR
```

Figure S11: Code snippet from ABB RobotStudio software used to unscrew vial caps with the YuMi robot (see Step 6 in Figure 1, main text, also **Video 1**, 2 min 49 sec *et seq.*), illustrating the intuitive programming interface that is available to construct workflows that contain multiple operations.

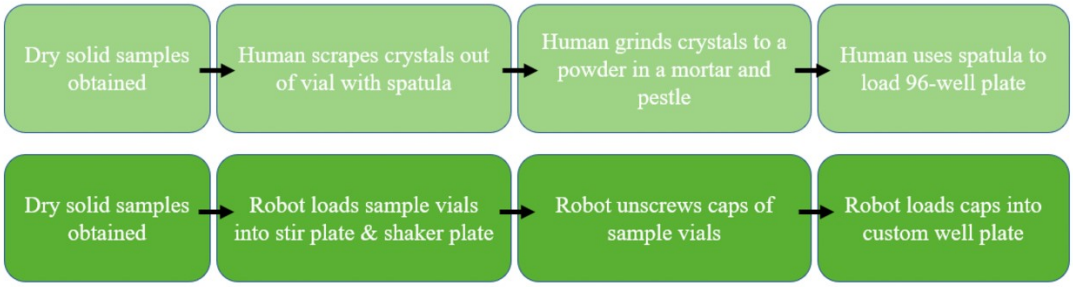

Figure S12: Schemes comparing typical human workflow (top) and autonomous robot workflow (bottom) for PXRD sample preparation.

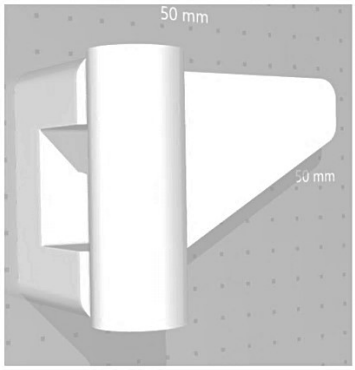

Figure S13: CAD file for handle modifications for the X-ray diffractometer doors; the triangular insert fits into a recess in the diffractometer doors, and this was the only physical modification made to the X-ray diffractometer, allowing the robot to open and close these doors reliably (**Video 1**, 4 min 52 sec *et seq.*) using the same end effector as used to manipulate the sample holders and PXRD platre. That the KUKA robot was, in fact, able to operate the diffractometer doors without any modification by using the existing recessed handles, but these simple 3D printed handle inserts made that process smoother and more robust.

Table S1: Summary of the unit cell parameters for benzimidazole obtained by Le Bail refinement (*1*) of the robotic and manual data using TOPAS academic (*2*), compared with the reported CSD (BZDMAZ01) unit cell parameters (*3*). Both PXRD datasets were collected in transmission mode over the range 4 to 40 degrees in 2θ in approximately 0.013 degree steps over 60 minutes.

	Robot-processed benzimidazole	**Manual benzimidazole**	**CSD reported benzimidazole**
***a* / Å**	13.6000(5)	13.4918(6)	13.507(10)
***b* / Å**	6.8564(2)	6.7985(6)	6.789(5)
***c* / Å**	6.9905(2)	6.9395(4)	6.940(5)
Space group	*Pna*2_1	*Pna*2_1	*Pna*2_1
R_{wp} **/ %**	4.69	19.21	N/A
χ^2	3.26	4.85	

Table S2: ROY samples were prepared in 20 mL glass vials at a total solution volume of 3 mL and left to evaporate to dryness in a fume cupboard.

Sample number	**Concentration of ROY in acetone (mg/mL)**	**Percentage of water in the crystallisation solution (% v/v)**
1	25	20
2	25	60
3	25	50
4	10	40
5	10	50
6	10	70
7	10	80
8	10	30

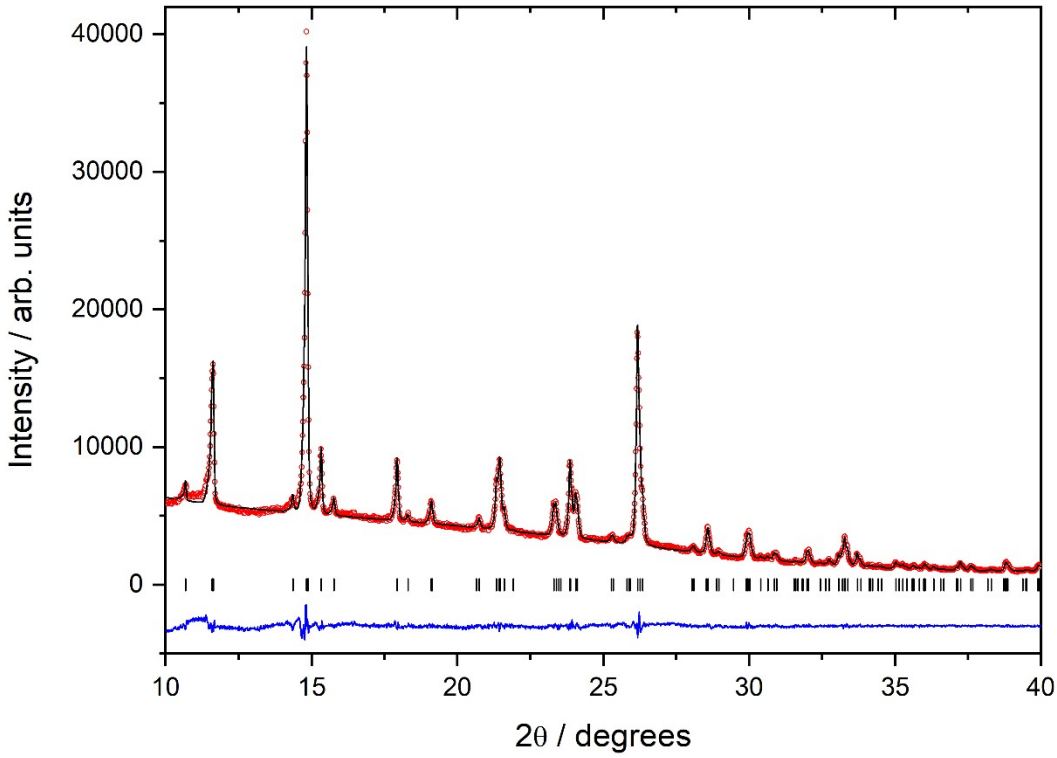

Figure S14: Final observed (red circles), calculated (black line) and difference (blue) profiles from Le Bail refinement (*1*) of the PXRD data obtained using TOPAS-Academic (*2*) from the robot-prepared sample 1 of ROY, as shown in Figure 4a. Tick marks indicate reflection positions. Note that both ROY and benzimidazole were used as supplied at commercial purity levels, so it is possible that low-level impurities may also exist in both cases.

Table S3: Summary of the unit cell parameters for ROY obtained by Le Bail refinement of the robotic and manual data, compared with the CSD reported (QAXMEH01) unit cell parameters (*4*).

	Robotic ROY	**Manual ROY**	**CSD reported ROY form Y**
***a* / Å**	8.6009(4)	8.6190(8)	8.5001(8)
***b* / Å**	16.5503(5)	16.449(1)	16.413(2)
***c* / Å**	8.5616(4)	8.5790(6)	8.5371(5)
***β* / °**	91.799(3)	91.859(6)	91.767(7)
Space group	$P2_1/n$	$P2_1/n$	$P2_1/n$
R_{wp} **/ %**	3.34	20.88	N/A
χ^2	2.06	10.82	

Table S4: Powder X-ray comparison of experimental data obtained from the automated workflow with simulated powder X-ray diffraction from crystal structure prediction datasets. The parameter VC-xPWDF gives a measure of dissimilarity between the experimental pattern and the simulated pattern from the CSP structure (lower values indicate a better match). The ranking of the known structure by PXRD similarity is given, along with the relative energy of the lowest energy CSP structure that has the lowest dissimilarity (VC-xPWDF) with respect to the correct structure from the CSP set. For context, 902 CSP structures over a 20 kJ mol^{-1} energy range were compared with experiment for benzimidazole. There were 264 CSP structures covering a 17.5 kJ mol^{-1} range for ROY. As such, all these matches are in the top few structures in the CSP landscapes, the single worst result being for Benzimidazole 4. In other cases, the method is soemwhat robust even to phase mixtures: for example, the Y polymorph of ROY was identified as the 9th best match in the CSP dataset for ROY 4, even though this sample is clearly a polymorph mixture (Figure 4b, main text).

sample	**VC-xPWDF**	**Rank by VC-xPWDF**	**Lowest energy false match, kJ mol^{-1}**
Benzimidazole 1	0.0085	1	–
Benzimidazole 2	0.0464	1	–
Benzimidazole 3	0.0710	6	5.34
Benzimidazole 4	0.1994	96	2.45
Benzimidazole 5	0.2256	24	2.56
Benzimidazole 6	0.1188	1	–
Benzimidazole 7	0.086	19	5.34
Benzimidazole 8	0.1139	2	2.71
ROY 1	0.0851	1	–
ROY 2	0.1683	27	0.82
ROY 3	0.1820	37	0.82
ROY 4	0.1852	9	5.69
ROY 5	0.2047	26	5.24
ROY 6	0.1306	4	6.80
ROY 7	0.1021	1	–
ROY 8	0.1165	1	–

5. Supporting References

1. A. Le Bail, H. Duroy, J. L. Fourquet, Ab-initio structure determination of LiSbWO6 by X-ray powder diffraction. *Mater. Res. Bull*. **23**, 447–452 (1988).
2. A. A. Coelho, *TOPAS and TOPAS-Academic*: an optimization program integrating computer algebra and crystallographic objects written in C++. *J. Appl. Cryst*. **51**, 210–218 (2018).
3. A. Escande, J. L. Galigné, Structure cristalline du benzimidazole, $C_7N_2H_6$: comparaison des résultats de deux études indépendantes. *Acta Cryst B*. **30**, 1647–1648 (1974).
4. L. Yu, G. A. Stephenson, C. A. Mitchell, C. A. Bunnell, S. V. Snorek, J. J. Bowyer, T. B. Borchardt, J. G. Stowell, S. R. Byrn, Thermochemistry and conformational polymorphism of a hexamorphic crystal system. *J. Am. Chem. Soc.* **122**, 585–591 (2000).
5. Beran, G. J. O., Sugden, I. J., Greenwell, C., Bowskill, D. H., Pantelides, C. C. & Adjiman, C. S. How many more polymorphs of ROY remain undiscovered. *Chem. Sci*. **13**, 1288 (2022).
6. Frisch, M. J. et al., Gaussian09 Revision D.01 (Gaussian Inc.) (2013).
7. Stone, A. J. Distributed multipole analysis: stability for large basis sets. *J. Chem. Theory Comput*. **1**, 1128-1132 (2005).
8. Ferenczy, G. G. Charges derived from distributed multipole series. *J. Comput. Chem*. **12**, 913-917 (1991).
9. Coombes, D. S., Price, S. L., Willock, D. J. & Leslie, M. Role of Electrostatic interactions in determining the crystal structures of polar organic molecules. a distributed multipole study. *J. Phys. Chem.* **100**, 7352-7360 (1996).
10. Price, S. L., Leslie, M., Welch, G. W. A., Habgood, M., Price, L. S., Karamertzanis, P. G. & Day, G. M. Modelling organic crystal structures using distributed multipole and polarizability-based model intermolecular potentials. *Phys. Chem. Chem. Phys.* **12**, 8478-8490 (2010).
11. Williams, D.E. & Cox, S. R. Nonbonded potentials for azahydrocarbons: The importance of the Coulombic interaction. *Acta Cryst. B* **40**, 404-417 (1984).
12. Stone, A. J. & Alderton, M. Distributed multipole analysis. methods and applications. *Mol. Phys.* **100**, 221-233 (2002).
13. Case, D. H., Campbell, J. E, Bygrave, P. J. and Day, G. M., *J. Chem. Theory Comput*. 2016, 12, 2, 910–924
14. Holden, J. R., Du, Z. & Ammon, H. L. Prediction of possible crystal structures for C-, H-, N-, O-, and F-containing organic compounds. *J. Comput. Chem*. **14**, 422-437 (1993).
15. Spek, A. L. Single-crystal structure validation with the program PLATON. *J. Appl. Cryst*. **36**, 7-13 (2003).
16. Chisholm, J. A. & Motherwell, S. COMPACK: A program for identifying structure similarity using distances. *J. Appl. Cryst*. **38**, 228-231(2005).
17. Kresse, G. & Furthmüller, J. Efficient iterative schemes for ab initio total-energy calculations using a plane-wave basis set. *Phys. Rev. B* **54**, 11169-11186 (1996).
18. Kresse, G. & Furthmüller, J. Efficiency of ab-initio total energy calculations for metals and semiconductors using a plane-wave basis set. *Comput. Mater. Sci*. **6**, 15-50 (1996).
19. Taylor, C. R. & Day, G. M. Evaluating the energetic driving force for cocrystal formation. *Cryst. Growth Des*. **18**, 892-904 (2018).

20. Grimme, S., Antony, J., Ehrlich, S. & Krieg, H. J. A consistent and accurate ab initio parametrization of density functional dispersion correction (DFT-D) for the 94 elements H-Pu. *Chem. Phys.* **132**, 154104 (2010).
21. Grimme, S., Ehrlich, S. & Goerigk, L. J. Effect of the damping function in dispersion corrected density functional theory. *Comput. Chem*. **32**, 1456– 1465 (2011).
22. Mayo, A. R., Marczenko, K. M. & Johnson E. R. Quantitative matching of crystal structures to experimental powder diffractograms. *Chem. Sci*. **14**, 4777 (2023).
23. David, W. I., Shankland, K., van de Streek, J., Pidcock, E., Motherwellb, W. D. S. & Cole, J. C. DASH: a program for crystal structure determination from powder diffraction data. *J. Appl. Cryst*. **39**, 910-915 (2006).

6. Code and Driver Repositories

The full software and drivers for the workflow can be found in the following repositories:

KUKA Sunrise programs: KUKA programs from SunriseOS for the new frames for the mobile robot operations developed in this project:

https://github.com/sgalunt/Thesis_Amy_Lunt/tree/main/Appendix%201%20KUKA%20code

ABB RobotStudio programs: Full ABB programs from RobotStudio for the YuMi dual-arm robot operations:
https://github.com/sgalunt/Thesis_Amy_Lunt/tree/main/Appendix%202%20YuMi%20code

ABB YuMi dual-arm robot driver:
https://github.com/sgalunt/Thesis_Amy_Lunt/blob/main/Appendix%203%20Drivers/yumi_driver.py

IKA stir plate driver:
https://github.com/sgalunt/Thesis_Amy_Lunt/blob/main/Appendix%203%20Drivers/ika_serial_driver.py

Panalytical PXRD driver:
https://github.com/sgalunt/Thesis_Amy_Lunt/blob/main/Appendix%203%20Drivers/pxrd_driver.py

ARChemist Process Files: Specifically, new files developed for this workflow:
https://github.com/sgalunt/Thesis_Amy_Lunt/tree/main/Appendix%204%20ARChemist%20code/Process%20Files

ARChemist Configuration Files:
https://github.com/sgalunt/Thesis_Amy_Lunt/tree/main/Appendix%204%20ARChemist%20code/Configuration%20Files

ARChemist Recipe Files:
https://github.com/sgalunt/Thesis_Amy_Lunt/tree/main/Appendix%204%20ARChemist%20code/Recipe%20Files